

RESEARCH LETTER

10.1002/2015GL065944

Special Section:

First Results from the MAVEN Mission to Mars

Key Points:

- The total ion escape rate is increased by an order of magnitude during the 8 March ICME
- The tailward ion loss is significantly increased at the ejecta phase
- There is no significant variation in the Martian ionosphere (at altitudes $\lesssim 200$ km)

Correspondence to:

C. Dong,
dcfy@umich.edu

Citation:

Dong, C., et al. (2015), Multifluid MHD study of the solar wind interaction with Mars' upper atmosphere during the 2015 March 8th ICME event, *Geophys. Res. Lett.*, 42, doi:10.1002/2015GL065944.Received 8 SEP 2015
Accepted 7 OCT 2015

Multifluid MHD study of the solar wind interaction with Mars' upper atmosphere during the 2015 March 8th ICME event

Chuanfei Dong^{1,2}, Yingjuan Ma³, Stephen W. Bougher¹, Gabor Toth¹, Andrew F. Nagy¹, Jasper S. Halekas⁴, Yaxue Dong⁵, Shannon M. Curry², Janet G. Luhmann², David Brain⁵, Jack E. P. Connerney⁶, Jared Espley⁶, Paul Mahaffy⁶, Mehdi Benna⁶, James P. McFadden², David L. Mitchell², Gina A. DiBraccio⁶, Robert J. Lillis², Bruce M. Jakosky⁵, and Joseph M. Grebowsky⁶¹Department of Climate and Space Sciences and Engineering, University of Michigan, Ann Arbor, Michigan, USA, ²Space Sciences Laboratory, University of California, Berkeley, California, USA, ³Institute of Geophysics and Planetary Physics, University of California, Los Angeles, California, USA, ⁴Department of Physics and Astronomy, University of Iowa, Iowa City, Iowa, USA, ⁵Laboratory for Atmospheric and Space Physics, University of Colorado Boulder, Boulder, Colorado, USA, ⁶NASA Goddard Space Flight Center, Greenbelt, Maryland, USA

Abstract We study the solar wind interaction with the Martian upper atmosphere during the 8 March 2015 interplanetary coronal mass ejection (ICME) by using a global multifluid MHD model. Comparison of the simulation results with observations from Mars Atmosphere and Volatile Evolution (MAVEN) spacecraft shows good agreement. The total ion escape rate is increased by an order of magnitude, from $2.05 \times 10^{24} \text{ s}^{-1}$ (pre-ICME phase) to $2.25 \times 10^{25} \text{ s}^{-1}$ (ICME sheath phase), during this time period. Two major ion escape channels are illustrated: accelerated pickup ion loss through the dayside plume and ionospheric ion loss through the nightside plasma wake region. Interestingly, the tailward ion loss is significantly increased at the ejecta phase. Both bow shock and magnetic pileup boundary (BS and MPB) locations are decreased from $(1.2R_M, 1.57R_M)$ at the pre-ICME phase to $(1.16R_M, 1.47R_M)$, respectively, during the sheath phase along the dayside Mars-Sun line. Furthermore, both simulation and observational results indicate that there is no significant variation in the Martian ionosphere (at altitudes $\lesssim 200$ km, i.e., the photochemical region) during this event.

1. Introduction

Unmagnetized planets, like Mars, are especially susceptible to atmospheric scavenging because the solar wind can interact directly with the upper atmosphere due to the lack of an intrinsic dipole magnetic field. Mars has crustal remanent magnetic fields, the strongest of which exist in the Southern Hemisphere and longitudes between 120° and 240°E [Acuña et al., 1999]. The highly localized crustal fields, combined with a weaker gravitational field and larger orbital eccentricity than Earth, leads to its unique solar wind interaction with the Martian upper atmosphere in the solar system [C. F. Dong et al., 2015].

On 18 November 2013, NASA launched the Mars Atmosphere and Volatile Evolution (MAVEN) spacecraft, and it successfully went into orbit at Mars on 21 September 2014. The goal of MAVEN is to understand the structure and composition of the Mars upper atmosphere and ionosphere, the nature of Mars' interaction with the solar wind, the current rate of escape of gases into space, and the role played by the Sun and the solar wind in controlling their variability [Bougher et al., 2014; Jakosky et al., 2015a]. These results will allow a better understanding of the role played by escape to space in the changes in the Mars climate through time [Jakosky et al., 2015a; Lillis et al., 2015]. Meanwhile, various plasma models based on different assumptions, i.e., test particle model [Curry et al., 2014, 2015a], multispecies MHD model [Ma et al., 2014, 2015], multifluid MHD model [Harnett and Winglee, 2006; Najib et al., 2011; Riouset et al., 2013, 2014; Dong et al., 2014], and kinetic hybrid model [Modolo et al., 2012; Brecht and Ledvina, 2014], have been developed and used to simulate the solar wind interaction with the Martian upper atmosphere and calculate the associated ion escape rates [Brain et al., 2010]. These models have also been used to place in context with the MAVEN observations [e.g., Curry et al., 2015b; Luhmann et al., 2015; Ma et al., 2015].

Recently, a powerful interplanetary coronal mass ejection (ICME) arrived at Mars at approximately 15:22 Universal Time (UT) on 8 March 2015, which drove a significant response from the Martian space plasma environment [Jakosky *et al.*, 2015b]. This paper aims to study the solar wind-Mars interaction during this event by using a global multifluid MHD model. In order to investigate and understand the Martian global response to this event, we did a detailed data-model comparison, mainly using data from the Solar Wind Ion Analyzer (SWIA) [Halekas *et al.*, 2015], the MAGnetometer (MAG) [Connerney *et al.*, 2015], and the Neutral Gas and Ion Mass Spectrometer (NGIMS) [Mahaffy *et al.*, 2014] instruments. We chose four cases to study. One is during a quiet period before the ICME (Case 1, pre-ICME phase), the other three are at different stages after the ICME arrival (Cases 2, early sheath phase; Case 3, late sheath phase; and Case 4, ejecta phase). The rest of this paper is arranged as described hereafter: In section 2, the 3-D Mars multifluid Block Adaptive Tree Solar wind Roe Upwind Scheme (BATS-R-US) magnetohydrodynamic code (MF-MHD) is briefly introduced together with the model inputs from instruments. In section 3, simulation results are presented and discussed based on the data-model comparison. The last section contains our conclusions and future work.

2. Model and Inputs

We only briefly introduce the 3-D Mars multifluid BATS-R-US MHD code use in this paper because the model has been described in detail previously [Glocer *et al.*, 2009; Najib *et al.*, 2011; Tóth *et al.*, 2012; C. F. Dong *et al.*, 2014, 2015]. By solving separate continuity, momentum, and energy equations for the four ion fluids H^+ , O^+ , O_2^+ , and CO_2^+ , the MF-MHD code can simulate the interplay between the Martian upper atmosphere and solar wind. The MF-MHD code can capture the feature of asymmetric dayside ion escape plumes, which have been observed by MAVEN [Y. Dong *et al.*, 2015; Brain *et al.*, 2015]. The lower boundary of the code is set at 100 km above the Martian surface, where the O^+ , O_2^+ , and CO_2^+ densities are taken to be the photochemical equilibrium values [Schunk and Nagy, 2009]. The velocity \mathbf{u} is set to satisfy a reflective boundary condition, which leads to approximately zero velocity at the inner boundary, as expected [Najib *et al.*, 2011; Dong *et al.*, 2014]. The model adopts a nonuniform, spherical grid with a radial resolution varying from 5 km at the lower boundary to 1000 km at the outer boundary (~ 20 Mars Radii, R_M) and with (both meridional and azimuthal) angular resolution varying from 1.5° to 3° . The code is run in the Mars-Solar-Orbital (MSO) coordinate system, where the x axis points from Mars toward the Sun, the z axis is perpendicular to the Martian orbital plane, and the y axis completes the right-hand system. The computational domain is defined by $-24R_M \leq X \leq 8R_M$; $-16R_M \leq Y, Z \leq 16R_M$. Given the high collision frequencies between different particle species, the plasma temperature is defined as $T_{\text{plasma}} \equiv T_{\text{ion}} + T_{\text{electron}} = 2T_{\text{ion}} = 2T_{\text{electron}} = 2T_{\text{neutral}}$ at the inner boundary. The chemical reaction calculations include charge exchange, photoionization, and electron impact ionization [Schunk and Nagy, 2009; Najib *et al.*, 2011; Dong *et al.*, 2014]. We adopt the 3-D neutral atmosphere profiles from the Mars global ionosphere-thermosphere model [Bougher *et al.*, 2015].

In order to evaluate the Martian response to different stages of the ICME, we studied four cases corresponding to four successive orbits, from orbit 848 (O848) to orbit 851 (O851). Case 1 corresponds to the pre-ICME condition, Cases 2 and 3 correspond to the early and late sheath phases (solar wind density, velocity, and interplanetary magnetic field (IMF) strength all increase, but the late sheath phase has the greatest compression), and Case 4 corresponds to the ejecta phase (maintain the strong field and solar wind velocity in the sheath phase, but the ion density drops down). The upstream solar wind density and velocity are taken from the SWIA instrument average over the time period when MAVEN was in the solar wind. The interplanetary magnetic field (IMF) is based on the MAG measurements averaged over the same time period. Table 1 summarizes the parameters used for the four cases. It is noteworthy that the solar wind and IMF inputs for the MF-MHD code are based on the average over the time period listed in the second row of Table 1, while the crustal field orientations are based upon the periapsis time of each orbit. We use the 60° harmonic expansion for the crustal magnetic field developed by Arkani-Hamed [2001] to describe the observed fields at Mars [Acuña *et al.*, 1999].

3. Results

3.1. Data-Model Comparison and Model Validation

In order to validate our model calculations, we first compared the MF-MHD simulation results with the MAVEN data. Since we ran four steady state cases, each simulation can produce the results along the MAVEN trajectories from orbit 848 (O848) to orbit 851 (O851). In Figure 1, simulation results from different cases are shown in different background colors. The magenta line shows the ICME arrival time ($\sim 15:22$ UT).

Table 1. Input Parameters and Calculated Ion Escape Rates for Different Cases (in $\times 10^{24} \text{ s}^{-1}$)

Simulation Cases (Orbit #)	Case 1 (O848)	Case 2 (O849)	Case 3 (O850)	Case 4 (O851)
Time Period ^a	11:30–11:45	16:25–16:55	20:45–21:15	01:10–01:30
N_{SW} (cm^{-3})	1.9	3.0	11.9	4.5
B_{IMF} (nT)	(–2.1,3.1,–1.0)	(–8.4,–3.3,–8.7)	(5.2,5.4,1.7)	(18.1,7.6,–0.8)
U_{SW} (km/s)	(–510.4,19.6,–5)	(–830,141,–18)	(–825,62.9,–5.8)	(–800,–45,–10)
Periapsis Time ^b	2015-03-08T13:22:53	2015-03-08T17:53:22	2015-03-08T22:23:53	2015-03-09T02:54:24
Subsolar position (longitude and latitude)	(81.86,–20.55)	(16.06,–20.52)	(–49.74,–20.49)	(–115.54,–20.46)
O^+ ion escape rate	0.60	0.72	1.92	0.92
O_2^+ ion escape rate	1.28	4.40	18.7	6.37
CO_2^+ ion escape rate	0.17	0.51	1.88	0.81
Total ion escape rate	2.05	5.62	22.5	8.10

^aThe solar wind and IMF inputs are based on the average over these four time periods. Given that the case studies here are based on steady state simulations, we slightly modified the solar wind and IMF parameters (<5%, except the change of $B_{\text{IMF},z}$ in Case 1 from –3.0 nT to –1.0 nT) in order to match the bow shock location. The solar wind variability makes the average values not necessarily the correct ones to use for our simulations, but overall the values listed above are close to the real solar wind and IMF data.

^bThe crustal field orientation is based on the periapsis time of each orbit.

Figure 1 (first panel) displays the MAVEN trajectories. The dash-dotted black, dashed green, and solid red curves represent the latitude, solar zenith angle, and altitude of MAVEN trajectories, respectively. These three parameters are adequate to locate the MAVEN position with respect to Mars. Figure 1 (second panel) compares the calculated ion densities (dashed black n_i and solid red $n_{\text{O}_2^+}$ curves) with the SWIA (dotted blue line) and NGIMS (magenta circle marker) densities, which are in good agreement. It is noteworthy that SWIA has no mass resolution [Halekas et al., 2015], so it cannot distinguish different ion species. In addition, only two orbits (O849 and O851) of the NGIMS ion densities were measured because the ion mode is turned on with the closed source mode (measuring, e.g., Ar, CO_2 , O_2 , NO, and He) on every other orbit [Mahaffy et al., 2014].

Figure 1 (third panel) compares the solar wind velocity from the SWIA instrument (solid line) with the MF-MHD results (dashed line), which again are quite consistent. The nearly perfect match for U_x indicates that the MF-MHD code captures the right bow shock location as observed by SWIA. Comparisons of the MF-MHD calculations (dashed line) and the MAG data (solid line) are shown in Figure 1 (fourth to sixth panels), which are also consistent with each other. The solid red curve (in Figure 1 seventh panel) represents the calculated Martian crustal field strength, demonstrating that the increase of magnetic field strength near periapsis is mainly caused by the localized crustal field. The good agreement between the MF-MHD calculations and MAVEN data in all panels of Figure 1 indicates that the MF-MHD model can reproduce most of the features observed by MAVEN, thus validating its estimate of ion escape rates that will be shown in the following paragraphs.

Figure 2 presents a detailed data-model comparison on the orbits where NGIMS ion data are available. All four simulation results along orbits 849 and 851 are plotted in Figure 2 in order to demonstrate the little influence of different ICME phases on the model ion distribution (at altitudes $\lesssim 200$ km, where the background ion density is very large) and its comparison with the data. Overall, the model results are consistent with the NGIMS data. The whole Martian ionosphere response to this ICME event, however, needs to be further investigated by a time-dependent simulation in a future study.

3.2. Ion Escape Plume and Ion Loss Rate

The multifluid MHD model can simulate the dayside ion escape plumes by considering the dynamics of individual ion species. The asymmetry is primarily caused by different Lorentz forces acting on each ion species. Combined with the generalized Ohm's law, the Lorentz force term in the ion momentum equations, $n_s q_s (\mathbf{u}_s \times \mathbf{B} + \mathbf{E})$, can be reformatted, among which the term $n_s q_s (\mathbf{u}_s - \mathbf{u}_+) \times \mathbf{B}$ is the main force to accelerate the planetary pickup ions and cause an asymmetric ion escape plume in the plane perpendicular to the magnetic field vector [Dong et al., 2014]. Here n_s , q_s , \mathbf{u}_s are the ion fluid number density, charge, and velocity of the species s , respectively. \mathbf{E} ($= -\mathbf{u}_+ \times \mathbf{B}$) and \mathbf{B} denote the electric and magnetic fields, and $\mathbf{u}_+ = \sum_s n_s q_s \mathbf{u}_s / (en_e)$ is the charge averaged ion velocity. The pickup ion first accelerated by the electric field $\mathbf{E} = -\mathbf{u}_+ \times \mathbf{B}$ and then deflected by the $\mathbf{u}_s \times \mathbf{B}$ force, the ion reaches (at most) twice the solar wind velocity (u_{sw}) before turning

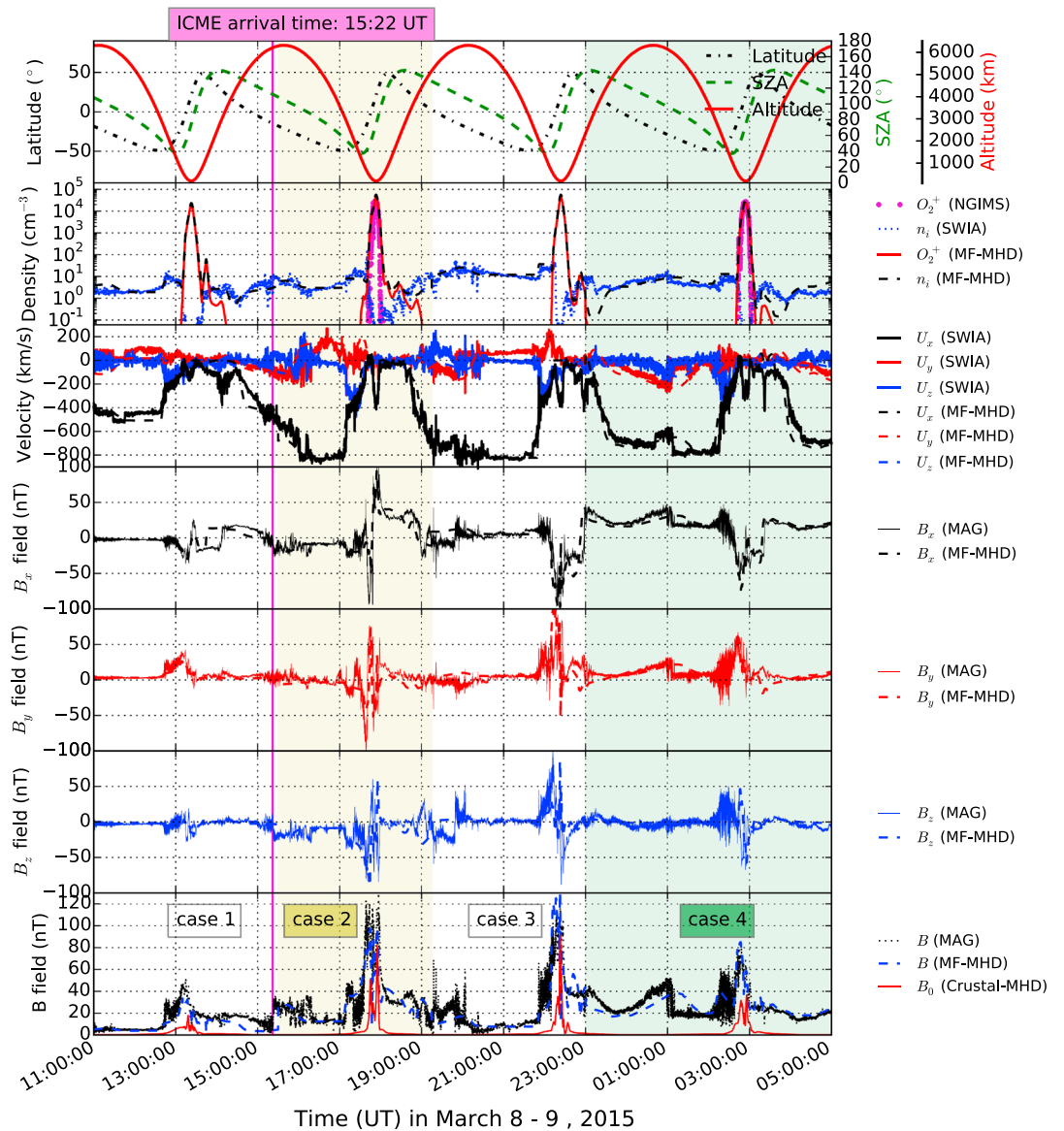


Figure 1. Data-model comparison of O_2^+ ion density, solar wind density and velocity, and magnetic field using the NGIMS, SWIA, and MAG data.

back and then being decelerated toward the cusp. Interestingly, it has been shown that a multifluid MHD model can partially reproduce some major features obtained with a hybrid code, such as the gyration of the planetary/cometary heavy ions and the associated pickup process [Rubin *et al.*, 2014]. The characteristic spatial scale, $\sim L_g$, associated with the asymmetry is controlled by the ratio $m_s u_{sw} / (q_s B)$ via dimensional analysis, at which the ion is fully picked up [Dong *et al.*, 2014]. In a kinetic particle model, this characteristic length is essentially the ion gyroradius [e.g., Dong *et al.*, 2013; Curry *et al.*, 2014], but it may not be appropriate to use this terminology in a code based on the fluid description. The heavier the ions (note $q_s = e$ in the model and $L_g \propto m_s$), the more significant the escape plume. Recently, the ion escape plume has been observed and verified using MAVEN measurements [Y. Dong *et al.*, 2015; Brain *et al.*, 2015]. Y. Dong *et al.* [2015] estimated the O^+ escape rate through the polar plume to be $\sim 35\%$ of the tailward escape and $\sim 25\%$ of the total escape for energies > 25 eV.

Figure 3 shows the contour plot of the O_2^+ ion speed, $U_{O_2^+}$, on an isosurface of O_2^+ ion density with $n_{O_2^+} = 0.005 \text{ cm}^{-3}$. It is well known that the dayside ion escape plume is a region filling with low-density and high-energy ion fluxes [Y. Dong *et al.*, 2015]. Isosurfaces with other $n_{O_2^+}$ values can show similar structures.

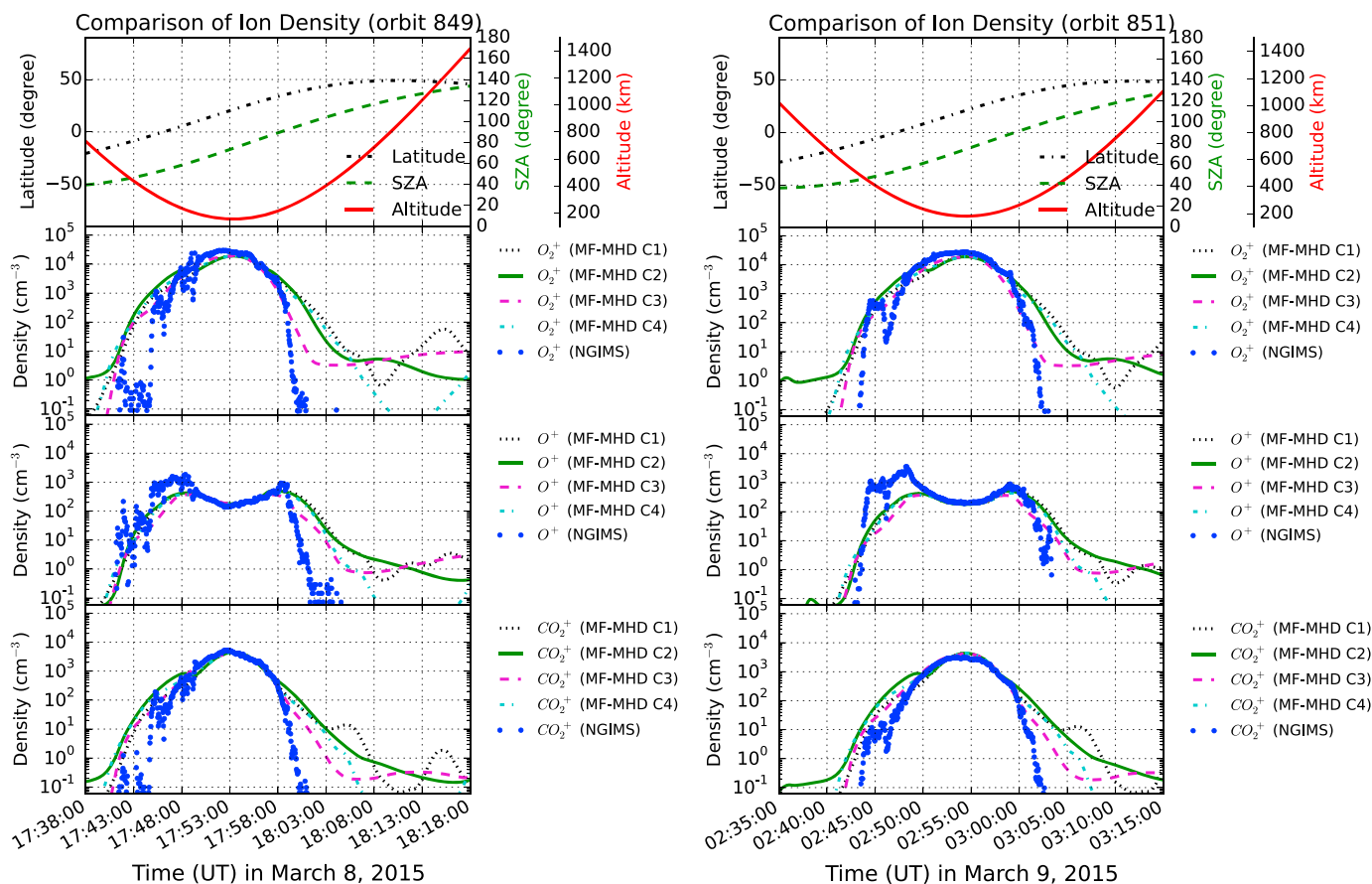


Figure 2. Data-model comparison of ionospheric ion density profiles by using NGIMS ion data. Case 1, black dotted curve; Case 2, solid green curve; Case 3, dashed magenta curve; and Case 4, dash-dotted cyan curve.

However, in order to evince the structure, $n_{O_2^+}$ cannot be too large. In addition, the O^+ and CO_2^+ ions also display similar asymmetric plume-shaped isosurfaces as that of O_2^+ ion. The $U_{O_2^+}$ -colored isosurfaces are illustrated for two purposes:

1. To show a global picture of the pickup ion acceleration. The color ($U_{O_2^+}$) variation along the isosurface indicates that the ions escaping from the dayside plume can be accelerated to a higher speed (thus energy) than those escaping from the nightside plasma wake region (at a constant altitude). This physical picture is further verified in Figure 4, where we plot both O_2^+ ion velocity vector in the x-z plane and its speed along two selected $U_{O_2^+}$ streamlines. As shown in Figure 4 (both the velocity vectors and speed curves), the escaping ion originated from dayside ionosphere can be accelerated to a higher speed (along the solid red streamline located in the escape plume region) than those originated from nightside ionosphere (along the dashed blue streamline located in the nightside plasma wake region). Compared with the pre-ICME phase, the ion acceleration is more significant in the sheath phase (Figure 4).
2. To reveal two main ion escape channels: accelerated pickup ion loss through the dayside plume and “cold” ionospheric ion loss through the nightside plasma wake region. The word cold in this paper means that the energy is low. Detailed case studies on the response of pickup ions to this ICME event can be found in Curry *et al.* [2015b] using a test particle code [Curry *et al.*, 2014].

Unlike previous studies [e.g., Najib *et al.*, 2011; C. F. Dong *et al.*, 2014, 2015], which assumed an idealized solar wind (U_x component only) and IMF (56° Parker spiral), we adopted actual solar wind and IMF measurements from SWIA and MAG. The orientation of the ion escape plume in a multifluid MHD code is mainly in the $\mathbf{E} = -\mathbf{u}_+ \times \mathbf{B}$ direction [Najib *et al.*, 2011]. In Figure 3, the dayside ion escape plume does not always originate from the geographical polar region; therefore, when the term “polar plume” is used, it is specified in the Mars-Sun electric field (MSE) coordinate system, where the electric field is always parallel to the z axis [Brain

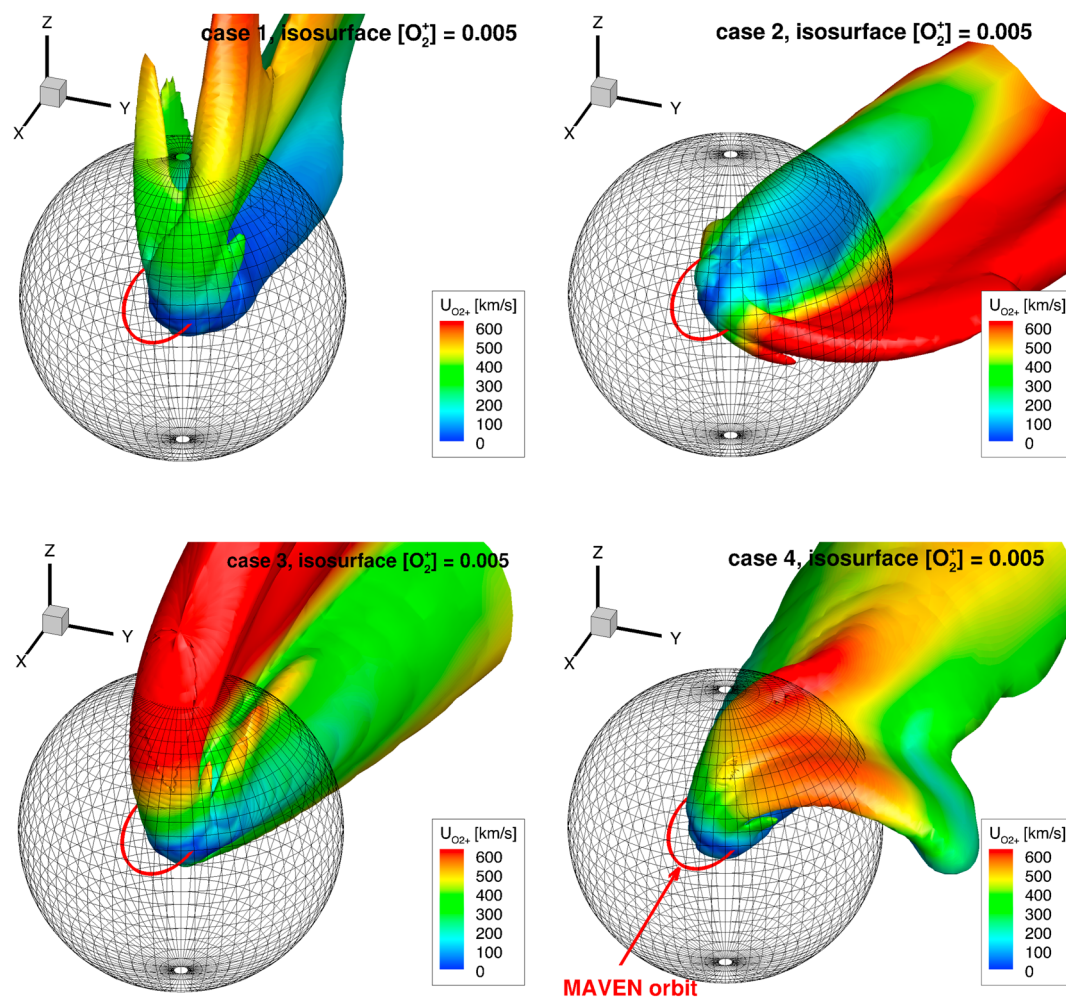


Figure 3. The isosurface of O_2^+ ion density with $n_{O_2^+} = 0.005 \text{ cm}^{-3}$, in which the contour of O_2^+ ion speed $U_{O_2^+}$ is presented. The meshed grid is the sphere with $r = 6R_M$ used to calculate the ion escape rate. The $r = 6R_M$ sphere in each plot is also used as a reference to know the relative size of the isosurface. The red curves are the MAVEN trajectories.

et al., 2015; *Curry et al.*, 2015b; *Y. Dong et al.*, 2015]. Compared with the pre-ICME phase (Case 1), the density isosurface of O_2^+ ion indicates that the ion escape is greatly enhanced during the ICME sheath phase (Case 3).

We summarize the calculated ion escape rates for all four cases by using a sphere with the radius equal to 6 Mars radii ($r = 6R_M$) in Table 1. Table 1 mirrors the enhancement of individual ion escape rates during the ICME event. The O^+ , O_2^+ , and CO_2^+ ion losses are, respectively, increased by factors of ~ 3.2 , ~ 14.6 , and ~ 11.1 , which result in an increase in the total ion escape rate by a factor of ~ 11 , from $2.05 \times 10^{24} \text{ s}^{-1}$ (Case 1, pre-ICME phase) to $2.25 \times 10^{25} \text{ s}^{-1}$ (Case 3, sheath phase), during this time period. Figure 4 shows the calculated O_2^+ ion number densities in the x - z plane. Inspection of Figure 4 reveals that the nightside ion escape is significantly increased in Case 3 compared to Case 1. The large fraction of tailward ion escape fluxes at the ejecta phase (Case 3) is mainly caused by two factors:

1. Compared with the pre-ICME phase (Case 1), the solar wind dynamic pressure was drastically intensified at the ejecta phase, leading to the largest solar wind proton density in the Martian upper atmosphere and the greatest compression of plasma boundaries (see Figure 5).
2. The IMF magnitude is significantly increased at the ejecta phase, thus the characteristic length, $L_g \propto u_{sw}/B$, associated with the asymmetry is decreased (refer to the isosurface shape illustrated in Figure 3). We plan to adopt the approach described in *Y. Dong et al.* [2015] to estimate the ion loss through the dayside escape plume and the nightside plasma wake in a future study.

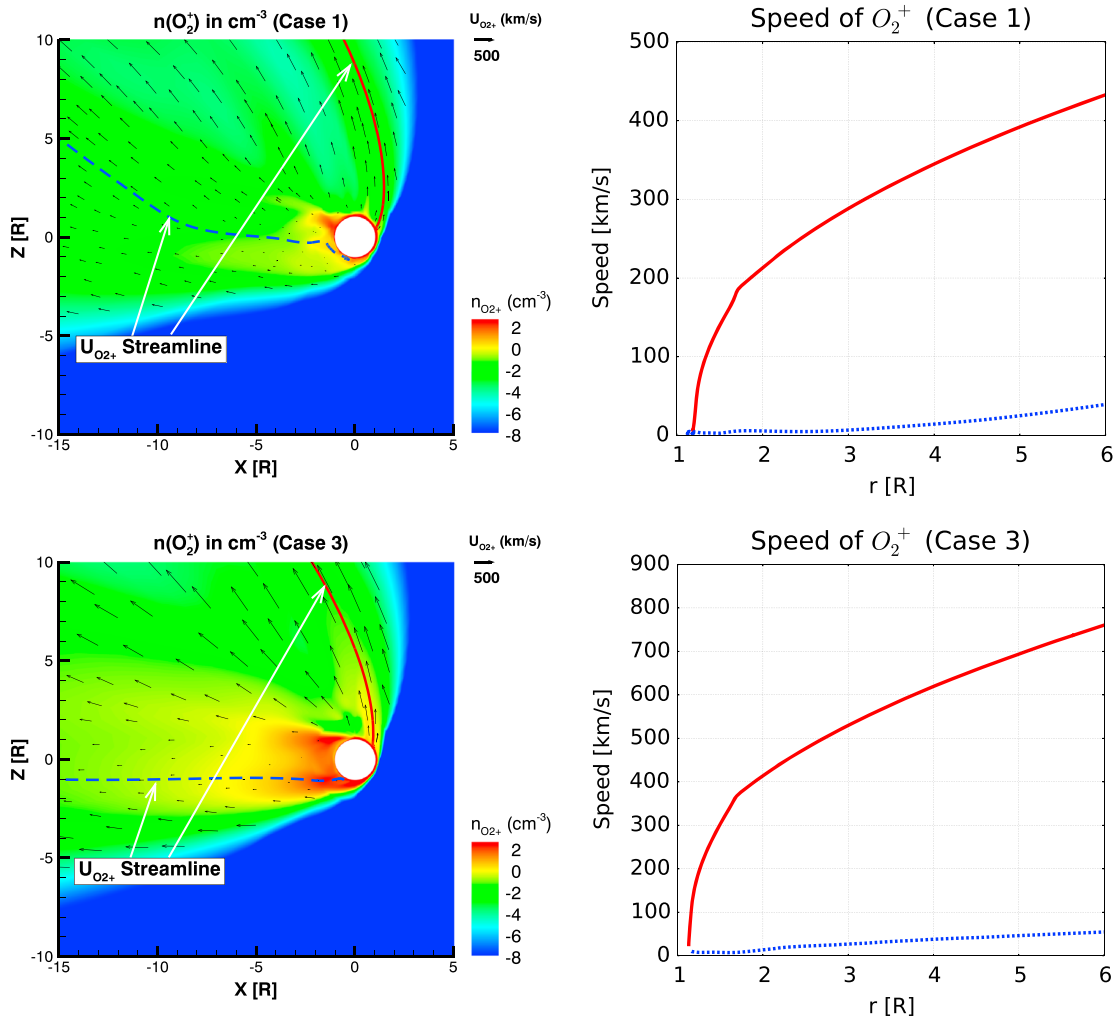


Figure 4. (left column) The calculated O_2^+ ion number densities in cm^{-3} in the x - z plane in a logarithmic scale (see density colorbar). The black arrow represents the O_2^+ ion velocity vector (a reference vector of 500 km/s magnitude is displayed in the upper right corner). The selected solid red and dashed blue curves in the contour plot are the $U_{O_2^+}$ streamlines at dayside escape plume and nightside plasma wake region, respectively. (right column) The corresponding speed (with same line style) along the streamline.

Brain *et al.* [2015] estimated a net ion escape rate of $\sim 2.5 \times 10^{24} s^{-1}$ by choosing a spherical shell at ~ 1000 km above the planet with energies >25 eV over a 4 month MAVEN period. It is interesting to mention that our model calculations for the pre-ICME case (which is close to the nominal solar wind condition) are in reasonable agreement with the ion escape rate estimated from available MAVEN data and previous estimates using the Mars Express data [Lundin *et al.*, 2013; Ramstad *et al.*, 2015] during this relatively weak solar cycle. The ion escape rates of Case 1 are further investigated by using selected spheres with different radii in order to demonstrate that the calculated ion escape rates do not change to any significant degree once the radius of the sphere exceeds $6 R_M$ (total ion escape rate, in $\times 10^{24} s^{-1}$, at a sphere of $3 R_M$: 2.22, $4 R_M$: 2.26, $5 R_M$: 2.12, $6 R_M$: 2.05, $7 R_M$: 2.04, $8 R_M$: 2.05, $9 R_M$: 2.06, $10 R_M$: 2.07; not listed in Table 1).

3.3. Variation of Plasma Boundaries at the Subsolar Region

Finally, we plot the pressure balance along the Mars-Sun line on the dayside for three case studies corresponding to three major ICME phases: pre-ICME phase (Case 1), sheath phase (Case 3), and ejecta phase (Case 4). Different pressures (the magnetic pressure, $P_b = B^2 / (2\mu_0)$, the dynamic pressure, $P_{dyn} = \rho v^2$, and the thermal pressure, $P_{th} = nk_B T$) are represented by different curves in Figure 5 (left column). The total thermal pressure, $P_{th(Tot)}$, by definition is the sum of $P_{th(SW)}$ and $P_{th(iono)}$; the latter peaks in the Martian ionosphere and is contributed by the planetary ions. It is noteworthy that in pre-ICME and sheath phases (Cases 1 and 3), the contribution of $P_{B(Tot)}$ to P_{total} is negligible in the upstream of Martian bow shock. The contribution of $P_{B(Tot)}$ to

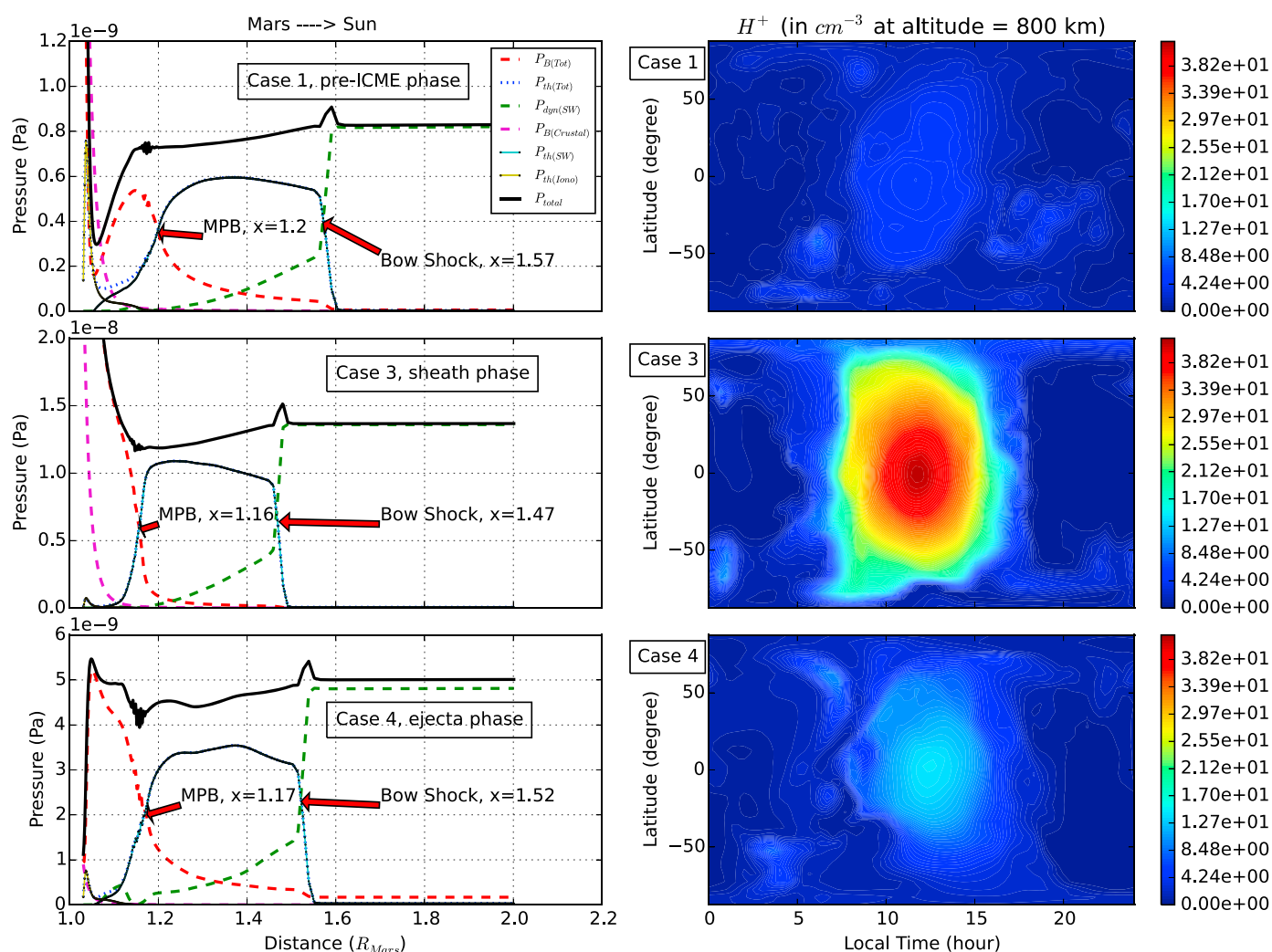


Figure 5. (left column) Pressure profiles along the Mars-Sun line (see top of the plot) on the dayside for Case 1 (pre-ICME phase), Case 3 (sheath phase), and Case 4 (ejecta phase). Different curves represent different pressures: the total magnetic pressure, $P_{B(Tot)}$ (dashed red), the total thermal pressure, $P_{th(Tot)}$ (dotted blue), the solar wind dynamic pressure, $P_{dyn(SW)}$ (dashed green), the crustal magnetic pressure, $P_{B(Crustal)}$ (dashed magenta), the solar wind thermal pressure, $P_{th(SW)}$ (solid cyan), the ionospheric thermal pressure, $P_{th(Iono)}$ (solid yellow), and the total pressure, P_{total} (solid black). (right column) The solar wind proton density profiles (in cm^{-3}) at altitude of 800 km for Cases 1, 3, and 4.

P_{total} in the ejecta phase (Case 4), however, cannot be ignored because of the strong IMF strength. Different from Case 4, $P_{B(Crustal)}$ increases dramatically near Mars (in Cases 1 and 3) due to the existence of strongly localized crustal magnetic fields, which helps the formation of strongly magnetized regions at Mars [Riouisset *et al.*, 2013, 2014].

By adopting the same approach in Najib *et al.* [2011], the intersection of $P_{dyn(SW)}$ and $P_{th(Tot)}$ is defined as the bow shock (BS) location, and the intersection of $P_{th(Tot)}$ and $P_{B(Tot)}$ is defined as magnetic pileup boundary (MPB). The BS and MPB positions are indicated by the red arrows in Figure 5. The bow shock location moves from $x = 1.57 R_M$ (Case 1) toward Mars at $x = 1.47 R_M$ (Case 3) due to the great enhancement of solar wind dynamic pressure. Compared with Case 3, the shock stand off distance, $x = 1.47 R_M$, slightly moves away from Mars in Case 4 mainly due to the sharp decrease of the ion density at the ejecta phase. The position of the magnetic pileup boundary follows a similar trend as that of the bow shock at the subsolar region: it first moves from $x_{cut} = 1.2 R_M$ (Case 1) to $x = 1.16 R_M$ (Case 3) and then slightly moves away from Mars and back to $x = 1.17 R_M$ (Case 4). The pressure balance in Figure 5 reveals the plasma boundary variations at the subsolar region during this event, but the behavior of these boundaries at the flanks may be different from those at the subsolar region.

Figure 5 (right column) displays the solar wind proton density (in cm^{-3}) at altitude of 800 km for Cases 1, 3, and 4. The largest density in Figure 5 (middle row; Case 3) indicates that the solar wind proton in the ICME late sheath phase can compress the boundaries downward more significantly than the other two cases, consistent with the results shown in Figures 4 and 5 (left panel).

4. Conclusion and Future Work

In summary, we studied the solar wind interaction with the Martian upper atmosphere during the 8 March ICME event based on four steady state case studies. These four cases correspond to three major ICME phases: pre-ICME phase (Case 1), sheath phase (Cases 2 and 3), and ejecta phase (Case 4). Detailed data-model comparisons demonstrate that the simulation results are in good agreement with the MAVEN measurements, indicating that the MF-MHD model can reproduce most of the features observed by MAVEN, thus providing confidence in the estimate of ion escape rates from its calculation. The total ion loss is significantly enhanced by a factor of ~ 11 , from $\sim 2.05 \times 10^{24} \text{ s}^{-1}$ (pre-ICME phase) to $\sim 2.25 \times 10^{25} \text{ s}^{-1}$ (sheath phase), during this time period. The acceleration of O_2^+ ions along the selected dayside and nightside ($\mathbf{U}_{\text{O}_2^+}$) streamlines demonstrates that the planetary ions escaping from the dayside plume have a higher speed (thus energy) than those escaping from the nightside plasma wake region. Two major ion escape channels are illustrated: accelerated pickup ion loss through the dayside plume and ionospheric ion loss through the nightside plasma wake region.

When solar wind dynamic pressure is increased and the characteristic length (or ion gyroradius in a kinetic description), $L_g \propto u_{\text{sw}}/B$, associated with the asymmetry is decreased, the ionospheric ion escaping from the plasma wake is significantly enhanced. Interestingly, by comparing all four simulation results along the same MAVEN orbit, we note that there is no significant variation in the Martian ionosphere (at altitudes $\lesssim 200$ km, i.e., the photochemical region). Finally, both bow shock and magnetic pileup boundary (BS and MPB) locations are decreased from $(1.2 R_M, 1.57 R_M)$ at the pre-ICME phase to $(1.16 R_M, 1.47 R_M)$, respectively, during the sheath phase along the dayside Mars-Sun line.

MAVEN has provided a great opportunity to study the evolution of the Martian atmosphere and climate over its history. A large quantity of useful data have been returned for future studies. These kinds of data-model comparisons can help the community to better understand the Martian upper atmosphere response to the (extreme) variation in the solar wind and its interplanetary environment from a global perspective. Further investigation on this ICME event will be implemented by a real-time study using a well-validated multispecies MHD (MS-MHD) code [Ma et al., 2014], which is computationally cheaper than the MF-MHD code by neglecting the individual ion dynamics. Although the MS-MHD code cannot reproduce the dayside ion escape plumes, the simulation based upon a real-time study is able to calculate the time-dependent escape rates of each ion species and reveal more details on how boundaries (i.e., bow shock and MPB) and Mars' ionosphere responses to the solar wind vary with time during this event.

References

- Acuña, M. H., et al. (1999), Global distribution of crustal magnetization discovered by the Mars global surveyor MAG/ER experiment, *Science*, 284, 790–793.
- Arkani-Hamed, J. (2001), A 50-degree spherical harmonic model of the magnetic field of Mars, *J. Geophys. Res.*, 106, 23,197–23,208.
- Bougher, S. W., T. E. Cravens, J. Grebowsky, and J. Luhmann (2014), The aeronomy of Mars: Characterization by MAVEN of the upper atmosphere reservoir that regulates volatile escape, *Space Sci. Rev.*, doi:10.1007/s11214-014-0053-7.
- Bougher, S. W., D. J. Pawlowski, J. M. Bell, S. Nelli, T. McDunn, J. R. Murphy, M. Chizek, and A. Ridley (2015), Mars global ionosphere-thermosphere model (MGITM): Solar cycle, seasonal, and diurnal variations of the Mars upper atmosphere, *J. Geophys. Res. Planets*, 120, 311–342, doi:10.1002/2014JE004715.
- Brain, D., et al. (2010), A comparison of global models for the solar wind interaction with Mars, *Icarus*, 206, 139–151.
- Brain, D. A., et al. (2015), The spatial distribution of planetary ion fluxes near Mars observed by MAVEN, *Geophys. Res. Lett.*, 42, doi:10.1002/2015GL065293.
- Brecht, S. H., and S. A. Ledvina (2014), The role of the Martian crustal magnetic fields in controlling ionospheric loss, *Geophys. Res. Lett.*, 41, 5340–5346, doi:10.1002/2014GL060841.
- Connerney, J. E. P., J. Espley, P. Lawton, S. Murphy, J. Odom, R. Oliverson, and D. Sheppard (2015), The MAVEN magnetic field investigation, *Space Sci. Rev.*, doi:10.1007/s11214-015-0169-4.
- Curry, S. M., M. W. Liemohn, X.-H. Fang, Y.-J. Ma, J. Slavin, J. Espley, S. Bougher, and C. F. Dong (2014), Test particle comparison of heavy atomic and molecular ion distributions at Mars, *J. Geophys. Res. Space Physics*, 119, 2328–2344, doi:10.1002/2013JA019221.
- Curry, S. M., J. G. Luhmann, Y. Ma, M. W. Liemohn, C. Dong, and T. Hara (2015a), Comparative pick-up ion distributions at Mars and Venus: Consequences for atmospheric deposition and escape, *Planet. Space Sci.*, doi:10.1016/j.pss.2015.03.026.
- Curry, S. M., et al. (2015b), MAVEN first results: The response of pick-up ions to the March 8th, 2015 ICME, *Geophys. Res. Lett.*, 42, doi:10.1002/2015GL065304.

Acknowledgments

This research was partially supported by NASA's MAVEN mission to Mars, and NASA Earth and Space Science Fellowship NNX13AO56H. We are grateful to the whole spacecraft team and instrument leads. The observational data used here are part of the MAVEN archive accessible through NASA's Planetary Data System. Resources supporting this work were provided by the NASA High-End Computing (HEC) Program through the NASA Advanced Supercomputing (NAS) Division at Ames Research Center. The Space Weather Modeling Framework that contains the BATS-R-US code used in this study is publicly available from <http://csem.engin.umich.edu/tools/swmf>. For distribution of the model results used in this study, please contact the corresponding author. C.F. Dong further acknowledge the useful discussions with Bart van der Holst and Michael Liemohn at the University of Michigan and Martin Rubin at the University of Bern, Switzerland.

- Dong, C. F., M. M. Cowee, and D. Winske (2013), Plasma and wave properties downstream of Martian bow shock: Hybrid simulations, *Rep. No. LA-UR 13-29060*, Los Alamos Natl. Lab. [Available at http://www.lanl.gov/projects/national-security-education-center/geophysics-planetary-physics/space-weather-school/_assets/docs/swx-report-2013.pdf.]
- Dong, C. F., S. W. Bougher, Y. Ma, G. Toth, A. F. Nagy, and D. Najib (2014), Solar wind interaction with Mars upper atmosphere: Results from the one-way coupling between the multifluid MHD model and the MTGCM model, *Geophys. Res. Lett.*, *41*, 2708–2715, doi:10.1002/2014GL059515.
- Dong, C. F., S. W. Bougher, Y. Ma, G. Toth, Y. Lee, A. F. Nagy, V. Tenishev, D. J. Pawlowski, M. R. Combi, and D. Najib (2015), Solar wind interaction with the Martian upper atmosphere: Crustal field orientation, solar cycle and seasonal variations, *J. Geophys. Res. Space Physics*, *120*, doi:10.1002/2015JA020990.
- Dong, Y., X. Fang, D. A. Brain, J. P. McFadden, J. S. Halekas, J. E. Connerney, S. M. Curry, Y. Harada, J. G. Luhmann, and B. M. Jakosky (2015), Strong plume fluxes observed by MAVEN: An important planetary ion escape channel, *Geophys. Res. Lett.*, *42*, doi:10.1002/2015GL065346.
- Glocer, A., G. Tóth, Y. J. Ma, T. I. Gombosi, J. C. Zhang, and L. M. Kistler (2009), Multifluid block-adaptive-tree solar wind roe-type upwind scheme: Magnetospheric composition and dynamics during geomagnetic storms—Initial results, *J. Geophys. Res.*, *114*, A12203, doi:10.1029/2009JA014418.
- Halekas, J. S., E. R. Taylor, G. Dalton, G. Johnson, D. W. Curtis, J. P. McFadden, D. L. Mitchell, R. P. Lin, and B. M. Jakosky (2015), The solar wind ion analyzer for MAVEN, *Space Sci. Rev.*, doi:10.1007/s11214-013-0029-z.
- Harnett, E. M. and R. M. Winglee (2006), Three-dimensional multifluid simulations of ionospheric loss at Mars from nominal solar wind conditions to magnetic cloud events, *J. Geophys. Res.*, *111*, A09213, doi:10.1029/2006JA011724.
- Jakosky, B. M., et al. (2015a), The Mars Atmosphere and Volatile Evolution (MAVEN) mission, *Space Sci. Rev.*, doi:10.1007/s11214-015-0139-x.
- Jakosky, B. M., et al. (2015b), MAVEN observations of the response of Mars to an interplanetary coronal mass ejection, *Science*, *348*, A09213, doi:10.1126/science.aad0210.
- Lillis, R. J., et al. (2015), Characterizing atmospheric escape from Mars today and through time, with MAVEN, *Space Sci. Rev.*, doi:10.1007/s11214-015-0165-8.
- Luhmann, J. G., et al. (2015), Implications of MAVEN Mars near-wake measurements and models, *Geophys. Res. Lett.*, *42*, doi:10.1002/2015GL066122.
- Lundin, R., S. Barabash, M. Holmström, H. Nilsson, Y. Futaana, R. Ramstad, M. Yamauchi, E. M. Dubinin, and M. Fraenz (2013), Solar cycle effects on the ion escape from Mars, *Geophys. Res. Lett.*, *40*, 6028–6032, doi:10.1002/2013GL058154.
- Ma, Y. J., X. Fang, C. T. Russell, A. F. Nagy, G. Toth, J. G. Luhmann, D. A. Brain, and C. Dong (2014), Effects of crustal field rotation on the solar wind plasma interaction with Mars, *Geophys. Res. Lett.*, *41*, 6563–6569, doi:10.1002/2014GL060785.
- Ma, Y. J., et al. (2015), MHD model results of solar wind interaction with Mars and comparison with MAVEN plasma observations, *Geophys. Res. Lett.*, *42*, doi:10.1002/2015GL065218.
- Mahaffy, P. R., et al. (2014), The neutral gas and ion mass spectrometer on the Mars atmosphere and volatile evolution mission, *Space Sci. Rev.*, doi:10.1007/s11214-014-0091-1.
- Modolo, R., G. M. Chanteur, and E. Dubinin (2012), Dynamic Martian magnetosphere: Transient twist induced by a rotation of the IMF, *Geophys. Res. Lett.*, *39*, L01106, doi:10.1029/2011GL049895.
- Najib, D., A. F. Nagy, G. Tóth, and Y. J. Ma (2011), Three-dimensional, multifluid, high spatial resolution MHD model studies of the solar wind interaction with Mars, *J. Geophys. Res.*, *116*, A05204, doi:10.1029/2010JA016272.
- Ramstad, R., S. Barabash, Y. Futaana, H. Nilsson, X.-D. Wang, and M. Holmström (2015), The Martian atmospheric ion escape rate dependence on solar wind and solar EUV conditions I: Seven years of Mars Express observations, *J. Geophys. Res. Planets*, *120*, 1298–1309, doi:10.1002/2015JE004816.
- Riouisset, J. A., C. S. Paty, R. J. Lillis, M. O. Fillingim, S. L. England, P. G. Withers, and J. P. M. Hale (2013), Three-dimensional multifluid modeling of atmospheric electrodynamics in Mars' dynamo region, *J. Geophys. Res. Space Physics*, *118*, 3647–3659, doi:10.1002/jgra.50328.
- Riouisset, J. A., C. S. Paty, R. J. Lillis, M. O. Fillingim, S. L. England, P. G. Withers, and J. P. M. Hale (2014), Electrodynamics of the Martian dynamo region near magnetic cusps and loops, *Geophys. Res. Lett.*, *41*, 1119–1125, doi:10.1002/2013GL059130.
- Rubin, M., et al. (2014), Plasma environment of a weak comet—Predictions for Comet 67P/Churyumov–Gerasimenko from multifluid–MHD and hybrid models, *Icarus*, *242*, 38–49.
- Schunk, R. W., and A. F. Nagy (2009), *Ionospheres*, 2nd ed., Cambridge Univ. Press, New York.
- Tóth, G., et al. (2012), Adaptive numerical algorithms in space weather modeling, *J. Comput. Phys.*, *231*, 870–903.